Modelling the multiwavelength light curves of PSR B1259-63/LS 2883 - II. The effects of anisotropic pulsar wind and Doppler-boosting

S. W. Kong[1,2], K. S. Cheng[2]

hrspksc@hkucc.hku.hk

and

Y. F .Huang[1,3]

Received _____; accepted _____

[1]Department of Astronomy, Nanjing University, Nanjing 210093, China

[2]Department of Physics, University of Hong Kong, Pokfulam Road, Hong Kong

[3]Key Laboratory of Modern Astronomy and Astrophysics (Nanjing University), Ministry of Education, Nanjing 210093, China

ABSTRACT

PSR B1259-63/LS 2883 is a binary system in which a 48-ms pulsar orbits around a Be star in a high eccentric orbit with a long orbital period of about 3.4 yr. It is special for having asymmetric two-peak profiles in both the X-ray and the TeV light curves. Recently, an unexpected GeV flare was detected by *Fermi* gamma-ray observatory several weeks after the last periastron passage. In this paper, we show that this observed GeV flare could be produced by the Doppler-boosted synchrotron emission in the bow shock tail. An anisotropic pulsar wind model, which mainly affects the energy flux injection to the termination shock in different orbital phase, is also used in this paper, and we find that the anisotropy in the pulsar wind can play a significant role in producing the asymmetric two-peak profiles in both X-ray and TeV light curves. The X-ray and TeV photons before periastron are mainly produced by the shocked electrons around the shock apex and the light curves after periastron are contributed by the emission from the shock apex and the shock tail together, which result in the asymmetric two-peak light curves.

Subject headings: binaries: close — gamma rays: stars — pulsars: individual(PSR B1259-63) — X-rays: binaries

1. Introduction

The discovery of the PSR B1259-63/LS 2883 system was first reported in 1992 (Johnston et al. 1992), and it is a binary system containing a rapidly rotating pulsar, PSR B1259-63, in orbit around a massive Be star companion LS 2883. The spin period of the pulsar is $P = 47.76$ ms and the spin-down luminosity is $L_{\rm sd} \simeq 8 \times 10^{35}$ ergs s^{-1}. The distance between the system and the Earth has been updated to be 2.3 ± 0.4 kpc by Negueruela et al. (2011) recently. The emission from this system has been widely detected in radio (Johnston et al. 2005), X-rays (Chernyakova et al. 2006, 2009; Uchiyama et al. 2009) and TeV gamma-rays (Aharonian et al. 2005, 2009), and the light curves are modulated on the orbital period. Especially, the X-ray and TeV light curves are similar and display two-peak profiles. Recently, this system was first detected in the GeV range by the *Fermi* satellite in its last periastron passage in 2010 mid-December (Abdo et al. 2011; Tam et al. 2011). An interesting GeV flare was observed with a cut-off energy at several hundred MeV, which is difficult to explain with the traditional lepton model.

In the traditional lepton model of gamma-ray binaries hosting a pulsar, the interaction between the pulsar wind and the stellar outflow will terminate the winds with a shock roughly at the position where the dynamical pressures of the pulsar wind and the stellar wind are in balance, and this shock can accelerate electrons to relativistic energies. These accelerated electrons around the shock apex will emit broadband nonthermal emission via a synchrotron process for the X-rays or an external inverse Compton (EIC) scattering of the thermal photons from the Be star for the TeV gamma-rays (Tavani & Arons 1997; Dubus 2006; Khangulyan et al. 2007; Takata & Taam 2009; Kong et al. 2011). The X-ray light curve reaches a maximum in flux at periastron in the simplest models, which is inconsistent with observations. Some authors used some revised leptonic models to explain the drop of photon flux towards periastron, for example by introducing some non-radiative losses of electrons (Kangulyan et al. 2007) or varying the microphysical parameters (Takata & Taam 2009; Kong et al. 2011). On the other hand, the synchrotron spectrum

has a maximum energy no more than 2.36×10^8 eV by equating the synchrotron cooling timescale with the particle acceleration timescale (see Sect. 2.4), which seems consistent with the *Fermi* observed GeV cut-off energy during the flare. But we should notice that if the acceleration efficiency is constant, the maximum energy from synchrotron radiation will not vary along with the orbital phase. If this energy corresponds to the cut-off energy in the flaring period, the spectra in other periods cannot be explained properly. The EIC process mainly contributes to the photons at above 1 GeV, and also cannot explain the observed flare.

Some previous studies suggested that the GeV flare could be produced by Doppler-boosting the synchrotron radiation (Kong et al. 2011; Tam et al. 2011). The interaction between winds in a binary system should produce a bow-like structure. Bogovalov et al. (2008, 2012) presented their hydrodynamic simulations of the interaction between the relativistic and nonrelativistic winds in the PSR B1259-63/LS 2883 system, using both the unmagnetized and magnetized, both the isotropic and anisotropic pulsar winds. They found that the bulk motion of the downstream pulsar wind electrons can be accelerated from a Lorentz factor ~ 1 around the shock apex to a very large Lorentz factor in the bow shock tail. Some previous works (Khangulyan et al. 2008; Dubus, Cerutti & Henri 2010) have used the relativistic Doppler-boosting effect to explain the emission in gamma-ray binaries. A similar effect should exist in the PSR B1259-63/LS 2883 system. With a large bulk Lorentz factor, the emission from the shock tail should be strongly beamed. When the line-of-sight is near the beaming direction, we can receive the boosted GeV flux, otherwise, the GeV photons disappear. Coincidentally, the true anomaly of the GeV flare ($110^o - 130^o$) is almost the same as the true anomaly corresponding to the direction of the Earth (130^o), where the effect of Doppler-boosting is the most significant. Tam et al. (2011) found that the flux of the *Fermi* observations in the flaring period is enhanced by a factor of 5-10, which suggests a Doppler factor of around 1.5-2. It is interesting to note that for the X-ray and TeV bands, the second peaks in the light curves are also around the GeV flaring period. Therefore these second peaks may be produced by the emission from the shock apex and the Doppler-boosted emission from the shock

tail together.

The two-peak profiles in both the X-ray and TeV light curves are also distinctive features of the PSR B1259-63/LS 2883 system. In addition to the extra-contribution from the Doppler-boosting effect, some other anisotropic structures in this system may play significant roles on this problem. Bogovalov & Khangoulian (2002) has suggested an anisotropic distribution of energy flux in the pulsar wind to interpret the torus and jet-like structures in the center of the Crab Nebula. We can imagine that the anisotropy of wind is a common phenomenon in pulsars, including PSR B1259-63. If the spin axis of the pulsar is not perpendicular to the orbital plane, as the pulsar moving around its companion star, the energy flux injecting to the termination shock will be modulated with respect to the orbital phase. This modulation has a two-peak profile and further produces asymmetric two-peak profiles in the observed light curves.

In this paper, we will use the Doppler-boosting effect to reproduce the flare in GeV light curve in detail. We will also use an anisotropic pulsar wind model, together with the Doppler-boosting effect, to explain the asymmetric two-peak profiles in both the X-ray and TeV light curves. A variation of the magnetization parameter σ with the distance to the pulsar suggested in our previous paper (Kong et al. 2011) is included in our calculations. The outline of our paper is as follows: in Section 2, we introduce our model in detail. We then present our results and the comparison with observations in Section 3. Our discussion and conclusion are presented in Section 4.

2. Model Description

In our model, the broadband emission of the PSR B1259-63/LS 2883 system is mainly from the shock-accelerated electrons, both around the shock apex and in the shock tail. Due to the interaction between the pulsar wind and the stellar wind, strong shocks will be formed, and the

electrons (and positrons) can be accelerated at the shock front of the pulsar wind. This shock will also compress the magnetic field in the pulsar wind. The shocked relativistic electrons move in the magnetic field and the photon field of the Be star, and emit synchrotron and IC radiation to produce the multiband emission.

2.1. Shock Geometry

As illustrated in Fig.1, the interaction between the pulsar wind and the stellar wind will form a shock with a hollow cone-like structure. The distance from the shock contact discontinuity in the shock apex to the pulsar can be determined by

$$r_{\rm s} = d\frac{\eta^{1/2}}{1+\eta^{1/2}}, \tag{1}$$

where d is the separation between the pulsar and its companion and η is the ratio of the momentum fluxes from the pulsar and the massive star. When the pulsar wind is isotropic, the value of η should be $L_{\rm sd}/c\dot{M}v_{\rm w}$, where c is the speed of light, $\dot{M}$ is the mass-loss rate of the massive star and $v_{\rm w}$ is the velocity of the stellar wind. The detail of the wind is presented in Kong et al. (2011). Away from the apex, the shock surface becomes a hollow cone. The half-opening angle of the shock contact discontinuity should be (Eichler & Usov 1993)

$$\theta = 2.1(1-\frac{\overline{\eta}^{2/5}}{4})\overline{\eta}^{1/3}, \tag{2}$$

where $\overline{\eta} = \min(\eta, \eta^{-1})$. In this work, because we use an anisotropic pulsar wind model (see Sec. 2.2), the value of η in the shock apex should vary in different orbital phases. However, as shown by Bogovalov et al. (2012), the effect of the anisotropic pulsar wind on the bow-shock structure is relatively moderate, i.e it can not obviously affect the geometry of the bow shock, so we use the mean value of $<\eta>$ to determine the location of the shock apex and the shape of the bow shock in our calculations. The anisotropy in the pulsar wind mainly affects the energy flux injection to

the termination shock, i.e. affects the bulk Lorentz factor of the unshocked pulsar wind (see Eq. (3)) and the downstream magnetic field (see Eq. (7)), in different orbital phases.

In our model, we approximate that the observed emission is mainly produced in two regions (as illustrated in Fig.1): (1) Region I around the shock apex. The bulk motion of the particle flow in this region is assumed non-relativistic, so the radiation is isotropic. (2) Region II in the shock tail. As the particle flow propagating away from the shock apex, the bulk Lorentz factor of the flow will be increased gradually from $\Gamma_{\rm min} \simeq 1$ in this region (Bogovalov et al. 2008, 2012). The bulk motion is mildly-relativistic and the emission should be beamed. When the line-of-sight is near the beaming direction, as illustrated in Fig. 1, we can receive the Doppler-boosted photons. Note that Eq.(2) introduced by Eichler & Usov (1993) is defined at a distance very far from the shock apex, where the moving directions of the unshocked pulsar and stellar winds are nearly parallel. As shown in Fig. 1, because the moving directions of the unshocked pulsar and stellar winds are not the same in Region II, the mean half-opening angle of the particle flow φ should be larger than the angle θ estimated in Eq.(2) and the angle between the direction of the stellar photons and the beaming direction should be $\sim \varphi - \theta$. In this case, even if the line-of-sight is in the beaming direction, the directions of photons before and after scattering are not the same, and the EIC process will not be completely suppressed. When the particle flow is very far from the shock apex and the massive star, it will deviate from the flow direction of Region II due to the effects of the orbital motion and the Coriolis forces (Bosch-Ramon & Barkov 2011). So in our work, we assume that the electrons beyond Region II do not contribute to the observed flux. The bulk Lorentz factor of the flow at the end of Region II is $\Gamma_{\rm max}$. We also assume that the electron numbers with different bulk Lorentz factors (from $\Gamma_{\rm min} \simeq 1$ to $\Gamma_{\rm max}$) are the same in calculating the synchrotron and EIC radiations.

2.2. Anisotropic Pulsar Wind

As suggested by Bogovalov & Khangoulian (2002), the distribution of energy flux in the pulsar wind should be anisotropic and the particle flux can be considered to be more or less isotropic. Defining the angle between the pulsar spin axis and the direction from the pulsar to the massive star as $\theta_{\rm PB}$, the expression of the bulk Lorentz factor of the pulsar wind in the upstream of the termination shock as a function of $\theta_{\rm PB}$ should be as following:

$$\gamma_1 = \gamma_0 + \gamma_{\rm m}\sin^2\theta_{\rm PB}, \tag{3}$$

where $\gamma_0 \approx 200$, $\gamma_{\rm m} \approx 10^6 - 10^7$. Then the isotropic particle flux could be described by

$$\dot{N} = \frac{L_{\rm sd}}{m_{\rm e}c^2(\gamma_0 + \frac{2}{3}\gamma_{\rm m})}, \tag{4}$$

where $m_{\rm e}$ is the rest mass of the electron. As the pulsar orbiting around the massive star, $\theta_{\rm PB}$ will be modulated on the orbital phase (See Fig. 2), and the characteristics of the pulsar wind in the termination shock will vary accordingly.

As shown in Khangulyan et al. (2011a, 2011b), the EIC cooling will reduce the Lorentz factor of the unshocked electrons. We will not consider this effect in our modelling, and the initial bulk Lorentz factor parameter of the unshocked pulsar wind $\gamma_{\rm m}$ should be higher if this effect is added. Note that because the pulsar wind bow shock is extended, we only obtain an upper limit of the wind anisotropy effect. But the two emission regions in our model are only a part of the whole bow shock, the effect of the extending bow shock is relatively moderate. On the other hand, we can vary the parameter $\theta_{\rm PB}$ to increase the effect of the anisotropic pulsar wind.

2.3. Magnetization Parameter

The magnetization parameter σ is defined as the ratio of the magnetic energy density and the particle kinetic energy density in the pulsar wind. As estimated in Kong et al. (2011), by using the

pulsar parameters of PSR 1259-63, the magnetization parameter at the light cylinder should be

$$\sigma_{\rm L} = \frac{B_{\rm L}^2/8\pi}{2\dot{N}_{e^\pm} m_{\rm e} c/r_{\rm L}^2} \sim 4.68\times10^4 (\frac{B_{\rm L}}{2.5\times10^4{\rm G}})^2 (\frac{r_{\rm L}}{2.3\times10^8{\rm cm}})^2 (\frac{N_{\rm m}}{10^4})^{-1} (\frac{\dot{N}_{\rm GJ}}{5.26\times10^{31}{\rm s}^{-1}})^{-1}, \quad (5)$$

where $B_{\rm L}$ is the magnetic field at the light cylinder, $r_{\rm L}$ is the radius of the light cylinder, $\dot{N}_{e^\pm} = N_{\rm m}\dot{N}_{\rm GJ}$, $N_{\rm m}$ is the $e^\pm$ multiplicity and $\dot{N}_{\rm GJ} \sim 5.26\times10^{31}(B/3\times10^{11}{\rm G})(P/47.762{\rm ms})^{-2}{\rm s}^{-1}$ is the Goldreich-Julian particle flow at the light cylinder. In outer gap models (e.g. Cheng, Ho & Ruderman 1986a, 1986b; Zhang & Cheng 1997; Takata, Wang & Cheng 2010), the multiplicity due to various pair-creation processes could reach $10^4 - 10^5$. Eq. (5) shows that the pulsar wind is Poynting-dominated at the light cylinder. In some studies of the Crab Nebula (Kennel & Coroniti 1984a, 1984b), the pulsar wind should be kinetic-dominated ($\sigma \sim 0.003$) at a distance of $r_{\rm s} \sim 3\times10^{17}$ cm from the pulsar. We can imagine that between the light cylinder and the termination shock, the magnetic energy will be gradually converted into the particle kinetic energy. In our previous work (Kong et al. 2011), we have already shown that a variation of magnetization parameter σ with the distance from the pulsar could help us to reproduce the two-peak profiles in light curves, and we will use the same variation in this work and describe it as

$$\sigma = \sigma_{\rm L}(\frac{r}{r_{\rm L}})^{-\alpha}, \quad (6)$$

where r is the distance from the pulsar, and the typical value of the index α is of the order of unity.

The downstream magnetic field in Region I could be described as (Kennel & Coroniti 1984a, 1984b)

$$B = \sqrt{\frac{L_{\rm sd}\sigma}{r_{\rm s}^2 c(1+\sigma)} \frac{\gamma_1}{\gamma_0 + \frac{2}{3}\gamma_{\rm m}} (1 + \frac{1}{u_2^2})}, \quad (7)$$

$$u_2^2 = \frac{8\sigma^2 + 10\sigma + 1}{16(\sigma+1)} + \frac{[64\sigma^2(\sigma+1)^2 + 20\sigma(\sigma+1) + 1]^{\frac{1}{2}}}{16(\sigma+1)}. \quad (8)$$

Because Region II is far from the shock apex and it is an oblique shock there, the magnetic field should be lower than that in Region I. We assume the ratio between the magnetic fields in the two emission regions does not change in different orbital phases, and the exact ratio is determined by fitting in our work.

2.4. Radiation Process

It is usually assumed that the unshocked cold electron pairs in the pulsar wind can be accelerated to a power-law distribution $\dot{Q}(\gamma_{\rm e}) \sim (\gamma_{\rm e}-1)^{-p}$ $(\gamma_{\rm e,min} < \gamma_{\rm e} < \gamma_{\rm e,max})$ in the termination shock front and be injected into the downstream post-shock flow, where p is the electron distribution index. The minimum Lorentz factor can be determined from the conservations of the total electron number $L_{\rm sd}/\gamma_1 m_{\rm e}c^2 = \int \dot{Q}(\gamma_{\rm e}){\rm d}\gamma_{\rm e}$ and the total electron energy $L_{\rm sd} = \int \dot{Q}(\gamma_{\rm e})\gamma_{\rm e} m_{\rm e}c^2 {\rm d}\gamma_{\rm e}$, and we can acquire $\gamma_{\rm e,min} = \gamma_1(p-2)/(p-1)$ for $p > 2$ (Kirk, Ball & Skjæraasen 1999). The maximum Lorentz factor $\gamma_{\rm e,max}$ can be determined by equating the cooling timescale of electrons with the particle acceleration timescale as the following form,

$$\gamma_{\rm e,max} = \sqrt{\frac{6\pi e\zeta}{\sigma_{\rm T}B}} \sim 1.17\times10^8 \zeta^{1/2} B^{-1/2}, \tag{9}$$

where e is the electron charge, $\sigma_{\rm T}$ is the Thompson scattering cross section, ζ is the acceleration efficiency which is usually less than unity. Hereafter the convention $Q_x = Q/10^x$ is adopted for the cgs units.

The electrons will lose their energies through the radiative or adiabatic cooling processes, and the evolved electron spectrum $n(\gamma_{\rm e}, t)$ can be obtained from the continuity equation of the electron distribution (Ginzburg & Syrovatshii 1964),

$$\frac{\partial n(\gamma_{\rm e},t)}{\partial t} + \frac{\partial \dot{\gamma}_{\rm e} n(\gamma_{\rm e},t)}{\partial \gamma_{\rm e}} = \dot{Q}(\gamma_{\rm e}), \tag{10}$$

where $\dot{\gamma}_{\rm e}$ is the total energy loss rate of the electrons and $\dot{Q}(\gamma_{\rm e})$ is the injection rate. The coefficient of the injection rate in Region I $\eta_{\rm I} = \dot{Q}(\gamma_{\rm e})/(\gamma_{\rm e}-1)^{-p}$ $(\gamma_{\rm e,min} < \gamma_{\rm e} < \gamma_{\rm e,max})$ can be calculated from $\dot{Q}_{\rm tot} = \int \dot{Q}(\gamma_{\rm e}){\rm d}\gamma_{\rm e}$, where $\dot{Q}_{\rm tot} = L_{\rm sd}/[4m_{\rm e}c^2(\gamma_0 + 2\gamma_{\rm m}/3)]$ by assuming the typical scale of the shock apex is $r_{\rm s}$ (Dubus 2006). We do not know the exact structure and physical conditions in Region II, so we assume the electron injection rates are the same in the two regions for simplicity. In this case, about half of the pulsar wind electrons are injected to the emission regions.

Because the cooling and dynamic flow timescales are much smaller than the orbital period in

the PSR B1259-63/LS 2883 system, we use $\partial n(\gamma_{\rm e},t)/\partial t = 0$ to calculate the electron distribution at a steady state and acquire (Khangulyan et al. 2007; Zabalza, Parades & Bosch-Ramon 2011)

$$n(\gamma_{\rm e}) = \frac{1}{|\dot{\gamma}_{\rm e}|}\int_{\gamma_{\rm e}}^{\gamma_{\rm e,max}} \dot{Q}(\gamma'_{\rm e}){\rm d}\gamma'_{\rm e}. \quad (11)$$

For a source with the dynamical timescale $\tau_{\rm dyn}$, the electron number at a given Lorentz factor that can accumulate in the source could be simply calculated by $\dot{Q}(\gamma_{\rm e}){\rm min}[\tau_{\rm c}(\gamma_{\rm e}),\tau_{\rm dyn}]$ (Moderski et al. 2005), where $\tau_{\rm c}$ is the cooling timescale. Usually it is assumed the dynamical timescale in Region I is $\tau_{\rm dyn} = 3r_{\rm s}/c$. We also assume the dynamical timescale in Region II is the same with that in Region I for simplicity. For the radiative cooling timescale $\tau_{\rm c}$, we use the method proposed by Moderski et al. (2005) to calculate

$$\tau_{\rm c}(\gamma_{\rm e}) = \frac{3m_{\rm e}c}{4\sigma_{\rm T}\gamma_{\rm e}U_B}/[1+\frac{U_*}{U_B}F_{\rm KN}(\gamma_{\rm e})], \quad (12)$$

where $U_B = B^2/8\pi$ is the magnetic energy density, $U_* = L_{\rm star}/4\pi cR^2$ is the seed photon energy density in Region I where $L_{\rm star}$ is the luminosity of the massive star and R is the distance between the emission region and the massive star, $F_{\rm KN} \simeq (1+b)^{-1.5}$ and $b = 4\gamma_{\rm e}(2.8kT_{\rm eff}/m_{\rm e}c^2)$ in Region I, where k is the Boltzmann constant and $T_{\rm eff}$ is the effective temperature of the star. In Region II, U_* and b should be reduced by a factor of D_*^2 and D_* respectively, where $D_* = 1/\Gamma(1-\beta\cos\theta_*)$ is the Doppler factor, Γ is the bulk Lorentz factor of the particle flow, $\beta = \sqrt{(\Gamma^2-1)}/\Gamma$ and θ_* is the angle between the direction of the stellar photons and the moving direction of the flow. Note that a mono-energetic photon distribution with energy $2.8kT_{\rm eff}$ is used here as a good approximation of the thermal distribution of the stellar photons (Moderski et al. 2005).

In our model, the multiband photons from the PSR B1259-63/LS 2883 system are produced by the synchrotron radiation and the EIC process of the shock-accelerated electrons. An anisotropic inverse-Compton radiation formula is used in our calculations, in which the radiation power at frequency ν from a single electron with Lorentz factor $\gamma_{\rm e}$ in the comoving frame is given

by (Aharonian & Atoyan 1981)

$$\frac{\mathrm{d}P_{\nu}^{\mathrm{EIC}}(\gamma_e,\cos\theta_{\mathrm{SC}})}{\mathrm{d}\Omega}=\frac{3\sigma_{\mathrm{T}}}{4\pi}\int_{\nu_{\mathrm{s,min}}}^{\infty}\mathrm{d}\nu_{\mathrm{s}}\frac{\nu f_{\nu_{\mathrm{s}}}^{\mathrm{STAR}}}{4\gamma_e^2\nu_{\mathrm{s}}^2}h(\xi,b_\theta), \tag{13}$$

$$h(\xi,b_\theta)=1+\frac{\xi^2}{2(1-\xi)}-\frac{2\xi}{b_\theta(1-\xi)}+\frac{2\xi^2}{b_\theta^2(1-\xi)^2}, \tag{14}$$

where h is the Planck constant, $\xi=h\nu/(\gamma_{\mathrm{e}}m_{\mathrm{e}}c^2)$, $b_\theta=2(1-\cos\theta_{\mathrm{SC}})\gamma_{\mathrm{e}}h\nu_{\mathrm{s}}/(m_{\mathrm{e}}c^2)$, $h\nu_{\mathrm{s}}\ll h\nu\leq\gamma_{\mathrm{e}}m_{\mathrm{e}}c^2b_\theta/(1+b_\theta)$, θ_{SC} is the angle between the injecting photons and the scattered photons, and is varied along with the orbital phase. In Region II, this angle in the comoving frame θ_{SC} can be related to that in the observer frame φ_{SC} by $1-\cos\theta_{\mathrm{SC}}=D_{\mathrm{obs}}D_*(1-\cos\varphi_{\mathrm{SC}})$ (Rybicki & Lightman 1979; Dubus, Gerutti & Henri 2010; Zdziarski et al. 2012), where $D_{\mathrm{obs}}=1/\Gamma(1-\beta\cos\theta_{\mathrm{obs}})$ is the Doppler factor and θ_{obs} is the angle between the line-of-sight and the moving direction of the flow, which is modulated on the orbital period. The flux density of the massive star photons $f_{\nu_{\mathrm{s}}}^{\mathrm{STAR}}$ should be $\pi(R_*/R_{\mathrm{I}})^2 2h\nu^3/c^2[\exp(h\nu/kT_{\mathrm{eff}})-1]$ and $\pi(R_*/R_{\mathrm{II}})^2 2D_*^2h\nu^3/c^2[\exp(D_*h\nu/kT_{\mathrm{eff}})-1]$ (Rybicki & Lightman 1979; Zdziarski et al. 2012) in Region I and Region II respectively, where R_* is the radius of massive star, R_{I} and R_{II} are the distances between the emission regions and the massive star in Region I and Region II respectively. Because we do not know the exact structure of Region II, we use a mean value of $<R_{\mathrm{II}}>$ in our calculations. Note that here the massive star is assumed to be a black body emitter for simplicity.

The radiation from the electrons in both the shock apex and the shock tail are included in our calculations. The emission in the shock apex is assumed isotropic, and the radiation in the shock tail is beamed. For a point-like source, the Doppler-boosting effect will increase the photon energy by a factor of D_{obs} and increase the detected flux by a factor of D_{obs}^3 (Dubus, Gerutti & Henri 2010). We treat Region II as a ring-like shape on the cone-like termination shock approximation and we integrate over the different parts of Region II to get a more accurate result. According to Eq.(9), the synchrotron spectrum will cut off at the energy of

$$h\nu_{\mathrm{syn,max}}(\theta_{\mathrm{obs}})=D_{\mathrm{obs}}(\theta_{\mathrm{obs}})\frac{3he\gamma_{\mathrm{e,max}}^2B}{4\pi m_{\mathrm{e}}c}\sim 2.36\times10^8\zeta D_{\mathrm{obs}}(\theta_{\mathrm{obs}})\mathrm{eV}. \tag{15}$$

The variation of $D_{\rm obs}$ will help us to obtain the observed cut-off energy in the flaring period and the flare structure in the light curve.

3. Results

In this section, we will present some calculated results using our model, and compare them with the observations. We use the updated parameters for the PSR B1259-63/LS 2883 system in our calculations as follows (Negueruela et al. 2011): For the orbital parameters, we take the eccentricity $e = 0.87$, the semimajor axis $a = 7$ AU; For the compact object PSR B1259-63, we take the spin-down luminosity $L_{\rm sd} = 8 \times 10^{35}$ erg s^{-1}; For the Be star LS 2883, we take the stellar luminosity $L_{\rm star} = 7.3 \times 10^4 L_\odot$, the stellar radius $R_* = 10 R_\odot$, the effective temperature of the star $T_{\rm eff} = 30000$ K. The distance between the system and the Earth is taken to be 2.3 kpc. The angle between the line-of-sight and the orbital plane is taken to be 65$^{\rm o}$, and the true anomaly corresponding to the direction of the Earth is taken to be 130$^{\rm o}$. The input parameters we used are as follows: The mean ratio of the momentum fluxes from the pulsar and the massive star is $< \eta >= 0.16$, which corresponds to the mass-loss rate of the massive star $\dot{M} \sim 2.6 \times 10^{-8}\ M_\odot$ yr^{-1} with a velocity of $v_{\rm w} \sim 10^8$ cm s^{-1}, which is consistent with the typical value of the polar wind in the Be star (Waters et al. 1988). The corresponding half-opening angle of the shock cone is $\theta \sim 58^{\rm o}$. We choose the half-opening angle of Region II $\varphi = 65^{\rm o}$, so that around the true anomaly 130$^{\rm o}$, we can receive strong beamed emission from the shock tail. The angle between the direction of stellar photons and the moving direction of the flow in Region II is taken as $\theta_* \sim \varphi - \theta$. The maximum bulk Lorentz factor contributing to the observed flux in the shock tail is $\Gamma_{\rm max} = 2.0$, the bulk Lorentz factor parameters of the unshocked pulsar wind are $\gamma_0 = 200$ and $\gamma_{\rm m} = 2.0 \times 10^6$, the true anomaly of the projection of the pulsar spin axis in the orbital plane is 20$^{\rm o}$, the angle between the pulsar spin axis and the orbital plane is 46$^{\rm o}$, the magnetization parameter at the light cylinder is $\sigma_{\rm L} = 8 \times 10^3$ (for $N_{\rm m} \sim 5.8 \times 10^4$) and the decay index is $\alpha = 1.1$, the electron distribution index

is $p = 2.1$, the acceleration efficiency is $\zeta = 0.36$. The ratio of magnetic fields between Region II and Region I is assumed to be 0.1. The mean distance between the massive star and Region II $< R_{\rm II} >$ is taken to be 2.0 times of the binary separation, which is consistent to the results in Bogovalov et al. (2008, 2012) for $\Gamma_{\rm max} = 2.0$. Note that by using the parameters introduced above, the dynamical timescale $\tau_{\rm dyn}$ in Region I is $\sim d/c$ and that in Region II is less than $\sim 2d/c$. The difference between these two timescales is small, so the assumption that these two regions have the same dynamical timescales in our calculations is reasonable. The periastron is taken to be at orbital phase ~ 0 throughout the paper.

In Fig. 2, we show the variations of the angle between the pulsar spin axis and the line joining the two stars $\theta_{\rm BP}$, the bulk Lorentz factor of the unshocked pulsar wind γ_1, the magnetization parameter at the termination shock σ, and the magnetic field around the shock apex B with respect to the orbital phase. We can see that because the pulsar spin axis is not perpendicular to the orbital plane, $\theta_{\rm BP}$ is modulated on the orbital phase. For the case that the true anomaly of the projection of the pulsar spin axis in the orbital plane is $20^{\rm o}$ and the angle between the pulsar spin axis and the orbital plane is $46^{\rm o}$, $\theta_{\rm BP}$ will reach the minimum and maximum of $46^{\rm o}$ and $134^{\rm o}$ at the true anomaly of $20^{\rm o}$ and $-160^{\rm o}$ respectively. By using the anisotropic energy flux injection of the pulsar wind described in Section 2.2, γ_1 will vary with respect to $\theta_{\rm BP}$ (See Eq. (3)) and reach the maximum when $\theta_{\rm BP} = 90^{\rm o}$ at the true anomaly of $-70^{\rm o}$ and $110^{\rm o}$. In this case a two-peak profile appears in the distribution of γ_1. This two-peak structure will affect the minimum Lorentz factor $\gamma_{\rm e,min}$ in the electron distribution, and further affects the electron number at a certain Lorentz factor. The two-peak distribution on the electron number at a certain Lorentz factor will help us to obtain the two-peak profiles in light curves. We can also see that the magnetization parameter at the termination shock σ is modulated with respect to orbital phase, which is due to the different shock distance $r_{\rm s}$ in different orbital phases. The magnetic field in the shock apex B is also modulated with respect to orbital phase, which is similar to the modulation of magnetization parameter σ. But this modulation is not symmetrical because of the anisotropy of the pulsar wind (See Eq. (3)

and Eq. (7)).

Here we use the parameters introduced above to calculate the spectra and the comparisons with observations are shown in Fig. 3. The related timescales are shown in Fig. 4. It can be seen that our calculated X-ray and GeV emission is mainly produced by the synchrotron radiation and the TeV photons are mainly contributed by the EIC effect where the relativistic shocked electrons up-scatter the soft photons from the massive star. The X-ray and TeV flux at true anomaly of 120^{o} is contributed by the emission from shock apex and shock tail together, but the flux at true anomaly of -60^{o} is mainly produced by the electrons in the shock apex. By choosing the acceleration parameter $\zeta = 0.36$ in our modelling, the cut-off energy of the synchrotron spectrum in the unboosted region is $h\nu_{\rm syn,max} \sim 84$ MeV, which is a little lower than the lower limit of the energy range of the observations (100 MeV). So in the lower panel of Fig. 3, the pre-periastron synchrotron spectrum only have a small contribution in the above 100 MeV range. In the upper panel of Fig. 3, the line-of-sight is near the beaming direction. The photon flux and the photon energy will be strongly Doppler-boosted, and the cut-off energy in the synchrotron spectrum could be boosted to $h\nu_{\rm syn,max} \sim 300$ MeV, consistent with the *Fermi* observed GeV cut-off energy during the flare (Abdo et al. 2011; Tam et al. 2011). In this case, the observed flare can be reproduced. Unlike in the synchrotron component above 100 MeV, the EIC component above 1 TeV is not dominated by the boosted emission from the shock tail in the upper panel of Fig. 3. This is because (1) in the comoving frame the seed photon density in the shock tail is lower than that in the shock apex reduced by the Doppler de-boosting; (2) because of the anisotropy of the EIC emission, the flux will be suppressed when the angle between the directions of the input and output photons is small. In Fig. 4, we can see that the radiative cooling of the electrons with Lorentz factor $10^5 - 10^6$ is mainly dominated by the EIC radiation in the Klein-Nishina (KN) regime, and the radiative cooling of the electrons with higher energies is dominated by the synchrotron radiation. In our calculations, the minimum Lorentz factor of the shocked electrons is $\sim 10^5\gamma_{1,6}$, so the EIC process will never be in the Thomson regime. As a result, the synchrotron component

is higher than the EIC component in our calculated spectra. Our calculated synchrotron spectrum in the lower panel of Fig.3 does not fit the observations in the GeV range well, but note that the spectrum data in pre-periastron period given by different groups (Abdo et al. 2011; Tam et al. 2011) also are not consistent with each other, which may be due to the low value of the photon flux.

Our calculated broadband light curves of the PSR B1259-63/LS 2883 system and the comparisons with observations are presented in Fig. 5. We can see that the asymmetric two-peak profiles in the X-ray and TeV light curves can be well reproduced by our model. The observations before periastron are mainly contributed by the emission in the shock apex. The shock apex region also contributes to some emission in the post-periastron range, and the whole light curves display the asymmetric two-peak profiles with the flux before periastron higher than that after periastron. The anisotropic pulsar wind plays a significant role in producing this asymmetric two-peak profile because of its anisotropic energy flux injection to the termination shock. The emission from the shock tail is unimportant before periastron, because the angle between the line-of-sight and the direction of the flow in the shock tail $\theta_{\rm obs}$ is large. But it has an obvious contribution in the light curves after periastron, i.e. the second peaks in both the X-ray and TeV light curves are produced by the electrons in the shock apex and the shock tail together. For the GeV light curves, we can see that almost all the flux in the GeV flares are produced by the emission from the shock tail, where the emission is beamed and both the photon energy and detected flux are Doppler-boosted.

4. Conclusions and Discussion

The PSR B1259-63/LS 2883 system is an attractive binary system and special for having distinct modulations in the light curves of different energy bands. The X-ray and TeV light curves are similar and have two peaks before and after periastron respectively. The GeV light curve has an interesting flare several weeks after the periastron passage, whose spectrum cuts off at several

hundred MeV. In this paper, we have modelled the X-ray, GeV and TeV observations of this system. In our calculations, an anisotropic pulsar wind model and the relativistic Doppler-boosting effect are considered, and the X-ray and GeV photons are mainly from the synchrotron radiation and the TeV emission is mainly from the EIC process. We also assume that the emission from both the shock apex and the shock tail can contribute to the observations, and the shock apex radiation is isotropic and the emission from the shock tail is beamed because of the flow in the tail moving mildly-relativistically. We find that for the X-rays and TeV gamma-rays, the anisotropic energy flux injection of the pulsar wind plays an important role in producing the asymmetric two-peak profiles in the light curves. The observations before the periastron are mainly produced by the shocked electrons around the shock apex and the photons after periastron are contributed by the emission from the shock apex and the shock tail together. For the GeV gamma-rays, the observed flare is contributed by the emission from the shock tail, where the synchrotron photons are Doppler-boosted strongly. Unfortunately, we do not know the exact structure and physical processes in the shock tail, so in our calculations we make some assumptions, and we just show that our model is a possible way to reproduce the multiwavelength features in the PSR B1259-63/LS 2883 system. A more exact modelling could be done by using the detailed simulation results on binary pulsar systems (Bogovalov et al. 2008, 2012; Takata et al. 2012).

In our modelling, we use an assumption that the magnetization parameter σ varies with the distance to the pulsar, which is in principle possible. Some recent studies found that the variation of magnetization parameter σ could be in a different way. For example, Aharonian, Bogovalov & Khangulyan (2012) showed that the magnetization parameter σ should decrease abruptly within 10^{10} cm from the pulsar by fitting the observations of the Crab pulsar. Because the exact conversion process from Poynting flux to kinetic energy in the pulsar wind is still unclear, we think both models cannot be excluded. Some previous models implied that the energy conversion could exist over the entire distance from the pulsar to the termination shock (Coroniti 1990; Lyubarsky & Kirk 2001), and Contopoulos & Kazanas (2002) further showed that σ could decrease inversely

proportional to the distance from the light cylinder. In our previous paper (Kong et al. 2011), a variation of the magnetization parameter σ with the distance from the pulsar could help us to reproduce the two-peak profiles in light curves, and we also need a variation index $\alpha = 1.1$ to fit the observations better in this work. The adoption of $\alpha = 1.1$ here is purely phenomenological, which is affected by both the unclear magnetic energy dissipation and the EIC cooling of the unshocked pulsar wind (Khangulyan et al. 2011a, 2011b).

In our previous paper (Kong et al. 2011), we discussed the effect of the disk in the stellar wind on the X-ray and TeV light curves. The existence of a disk in the PSR B1259-63/LS 2883 system was confirmed by the radio observations (Johnston et al. 1996, 2005), but the exact position of the disk is still unclear. Some radio observations suggested that the disk is tilted with respect to the orbital plane and the line of intersection between the disk plane and the orbital plane is oriented at about $90^{\rm o}$ with respect to the major axis of the binary orbit (Wex et al. 1998; Wang, Johnston & Manchester 2004). Chernyakova et al. (2006) further suggested that the half-opening angle of the disk (projected on the pulsar orbital plane) is $\Delta\theta_{\rm disk} \simeq 18^{\rm o}.5$, and the intersection between the stellar equatorial plane and the orbital plane is inclined at $\theta_{\rm disk} \simeq 70^{\rm o}$ to the major axis of the pulsar orbit by fitting the X-ray and TeV light curves. Our previous calculations (Kong et al. 2011) showed that the X-ray flux increases in the passage of the disk, but the flux in the TeV range decreases significantly, which is consistent with the analysis by Kerschhaggl (2011). But note that we only consider the emission from the shock apex in Kong et al. (2011). When the pulsar entering the disk, the mass flux density will increase by a factor of 30-100 (Waters et al. 1988). By assuming the stellar wind velocity reduced by a factor of 10, the momentum flux density ratio η will decrease by a factor of 3-10 in the disk. In this case, the half-opening angle of the emission region in the shock tail will decrease and the angle between the line-of-sight and the direction of the flow in the shock tail $\theta_{\rm obs}$ will increase. The effect of Doppler-boosting will be suppressed and the emission from shock tail will be reduced. We can see from Fig. 5 that there are only upper limits in GeV light curves between true anomaly $90^{\rm o}$ and $115^{\rm o}$. The non-detection

in this period may be due to the suppression of the shock tail emission in the disk. The TeV observations also show a reduction in flux during the estimated disk passage, which are consistent with the explanation that emission from both the shock apex (Kong et al. 2011) and the shock tail will decrease in the disk. In X-ray band, there are significant signals between true anomaly 90^o and 115^o. But note that the X-ray flux from the shock apex could increase in the passage of the disk (Kong et al. 2011). The increase of the shock apex emission and the decrease of the shock tail emission in the disk will compete with each other, and the total flux could have no significant change.

In a recent paper, Khangulyan et al. (2011a) investigated the emission spectrum produced by the EIC process of the unshocked pulsar wind. They argued that the gamma-ray flare in GeV band after the periastron can be explained by the EIC emission of the cold pulsar wind with the bulk Lorentz factor $\gamma \approx 10^4$. The Be star disk plays a significant role in producing GeV flare in their model. First, the radiation of the shocked stellar disk can provide a dense photon target for the EIC scattering (van Soelen & Meintjes 2011). Second, the strong ram pressure inside the disk makes the wind termination shock stand close to the pulsar, and then the EIC luminosity should be suppressed. When the pulsar escapes the disk, the unshocked pulsar wind zone towards the observer is significantly increased. Consequently, an enhancement of the gamma-rays will be observed. Although in our model the GeV flare is produced by the Doppler-boosted synchrotron radiation, the EIC process of the unshocked pulsar wind may also have some contributions. Note that in the pre-periastron spectrum data in Tam et al. (2011), the *Fermi* detected emission is concentrated in a narrow band between 1-25 GeV. The observed spectrum is different from the spectrum produced by synchrotron radiation, and is similar to the calculated spectra in Khangulyan et al. (2011a). If the data in this range is indeed correct, we argue that this part of GeV photons may be produced by the EIC process of the unshocked electrons before termination shock in the pulsar wind.

If the 3D structure of the shock is a simple hollow cone at the shock tail, we expect that two flares per orbital period will be observed when the angle between the line-of-sight and the orbital plane is smaller than the half-opening angle of the shock cone, and each flare can last for about $2/\Gamma$ orbital phase $\sim 12^{\circ}(\Gamma/10)^{-1}$, where Γ is the bulk Lorentz factor at the tail of the shock. Otherwise, when the line-of-sight is near the edge of the hollow cone or outside the hollow cone, as illustrated in Fig. 1, only one flare could be observed in the light curve. As the angle between the line-of-sight and the flow direction increasing, the flare will be smoother and disappear eventually. In principle, our model could be used in other similar gamma-ray binary systems in our Galaxy with different observational angles and distinct light curves.

We would like to thank the anonymous referee for stimulating suggestions that lead to an overall improvement of this study. We also would like to thank Y. W. Yu for helpful suggestions and discussion. This research was supported by a 2011 GRF grant of the Hong Kong Government under HKU700911p. YFH was supported by the National Natural Science Foundation of China (Grant No. 11033002) and the National Basic Research Program of China (973 Program, Grant No. 2009CB824800).

REFERENCES

Abdo, A. A., Ackermann, M., Ajello, M., et al. 2011, ApJ, 736, L11

Aharonian, F., Akhperjanian, A. G., Anton, G., et al. 2009, A&A, 507, 389

Aharonian, F., Akhperjanian, A. G., Aye, K. M., et al. 2005, A&A, 442, 1

Aharonian, F. A., & Atoyan A. M. 1981, Ap&SS, 79, 321

Aharonian, F. A., Bogovalov, S. V., & Khangulyan, D. 2012, Nature, 482, 507

Bosch-Ramon, V., & Barkov, M. V. 2011, MNRAS, 535, 20

Bogovalov, S. V., & Khangoulian, D. V. 2002, MNRAS, 336, L53

Bogovalov, S. V., Khangulyan, D. V., Koldoba, A. V., et al. 2008, MNRAS, 387, 63

Bogovalov, S. V., Khangulyan, D., Koldoba, A. V., et al. 2012, MNRAS, 419, 3426

Cheng, K. S., Ho, C., & Ruderman, M. 1986a, ApJ, 300, 500

Cheng, K. S., Ho, C., & Ruderman, M. 1986b, ApJ, 300, 522

Chernyakova, M., Neronov, A., Aharonian, F., et al. 2009, MNRAS, 397, 2123

Chernyakova, M., Neronov, A., Lutovinov, A., et al. 2006, MNRAS, 367, 1201

Contopoulos, I., & Kazanas, D. 2002, ApJ, 566, 336

Coroniti, F. V. 1990, ApJ, 349, 538

Dubus, G., 2006, A&A, 456, 801

Dubus, G., Gerutti, B., & Henri, G. 2010, A&A, 516, 18

Eichler, D., & Usov, V. 1993, ApJ, 402, 271

Ginzburg, V. L., & Syrovatskii, S. I. 1964, The Origin of Cosmic Rays (Macmillan)

Johnston, S., Ball, L., Wang, N., & Manchester, R. N. 2005, MNRAS, 358, 1069

Johnston, S., Manchester, R. N., Lyne, A. G., et al., 1992, ApJ, 387, L37

Johnston, S., Manchester, R. N., Lyne, A. G., et al., 1996, MNRAS, 279, 1026

Kennel, C. F., & Coroniti, F. V. 1984a, ApJ, 283, 694

Kennel, C. F., & Coroniti, F. V. 1984b, ApJ, 283, 710

Kerschhaggl, M. 2010, A&A, 525, 80

Khangulyan, D., Aharonian, F. A., Bogovalov, S. V., & Ribó, M. 2011a, arXiv:1107.4833

Khangulyan, D., Aharonian, F. A., Bogovalov, S. V., & Ribó, M. 2011b, ApJ, 742, 98

Khangulyan, D., Hnatic, S., Aharonian, F., & Bogovalov, S. 2007, MNRAS, 380, 320

Khangulyan, D. V., Aharonian, F. A., Bogovalov, S. V., et al. 2008, IJMPD, 17, 1909

Kirk, J. G., Ball, L., & Skjæraasen, O. 1999, Astropart. Phys., 10, 31

Kong S. W., Yu, Y. W., Huang, Y. F., & Cheng, K. S. 2011, MNRAS, 416, 1067 (Paper I)

Lyubarsky, Y. & Kirk, J. G. 2001, ApJ, 547, 437

Moderski, R., Sikora, M., Coppi, P. S., & Aharonian, F. 2005, MNRAS, 363, 954

Negueruela, I., Ribó, M., Herrero, A., et al. 2011, ApJ, 732, L11

Rybicki G. B., & Lightman A. P. 1979, Radiative Processes in Astrophysics. Wiley, New York

Takata, J., Okazaki, A. T., Nagataki, S., et al. 2012, ApJ, 750, 70

Takata, J., & Taam, R. E. 2009, ApJ, 702, 100

Takata, J., Wang, Y., & Cheng, K. S. 2010, ApJ, 715, 1318

Tam, P. H. T., Huang, R. H. H., Takata, J., et al. 2011, ApJ, 736, L10

Tavani, M., & Arons, J. 1997, ApJ, 477, 439

Uchiyama, Y., Tanaka, T., Takahashi, T., et al. 2009, ApJ, 698, 911

van Soelen, B., & Meintjes, P. J. 2011, MNRAS, 412, 1721

Wang, N., Johnston, S., & Manchester, R. N. 2004, MNRAS, 351, 599

Waters, L. B. F. M., Taylor, A. R., van den Heuvel, E. P. J., et al. 1988, A&A, 198, 200

Wex, N, Johnston, S., Manchester, R. N., et al. 1998, MNRAS, 298, 997

Zabalza, V., Paredes, J. M., & Bosch-Ramon, V. 2011, A&A, 527, 9

Zdziarski, A. A., Sikora, M., Dubus, G., et al. 2012, MNRAS, 421, 2956

Zhang, L., & Cheng, K. S. 1997, ApJ, 487, 370

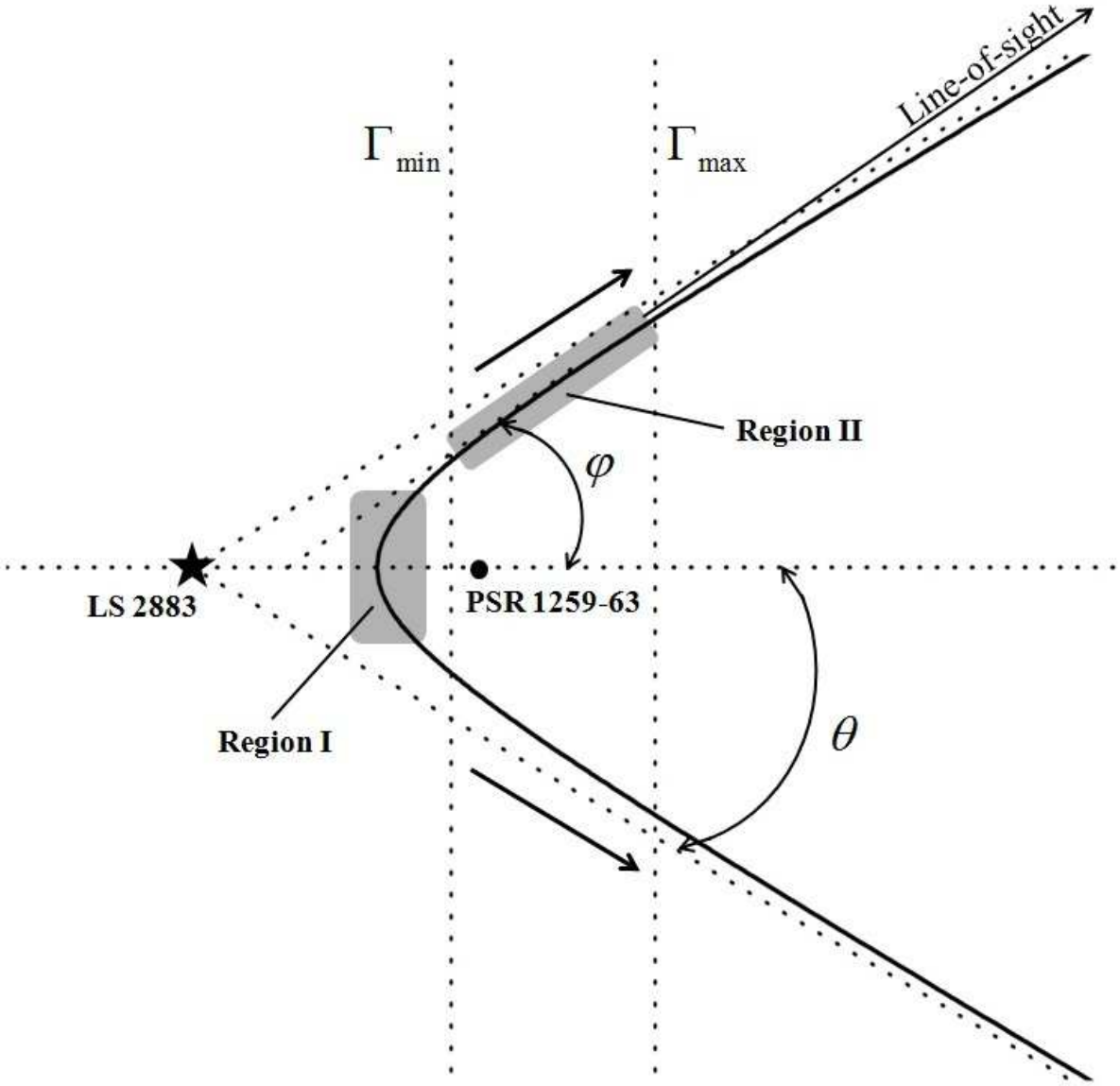

Fig. 1.— Geometry of the termination shock. The interaction between the pulsar wind and the stellar wind forms a termination shock with a hollow cone-like structure. Region I is around the shock apex, and the particle flow there is moving non-relativistically and radiating isotropically. Region II is in the shock tail, and the particle flow there is moving mildly-relativistically and the emission is beamed.

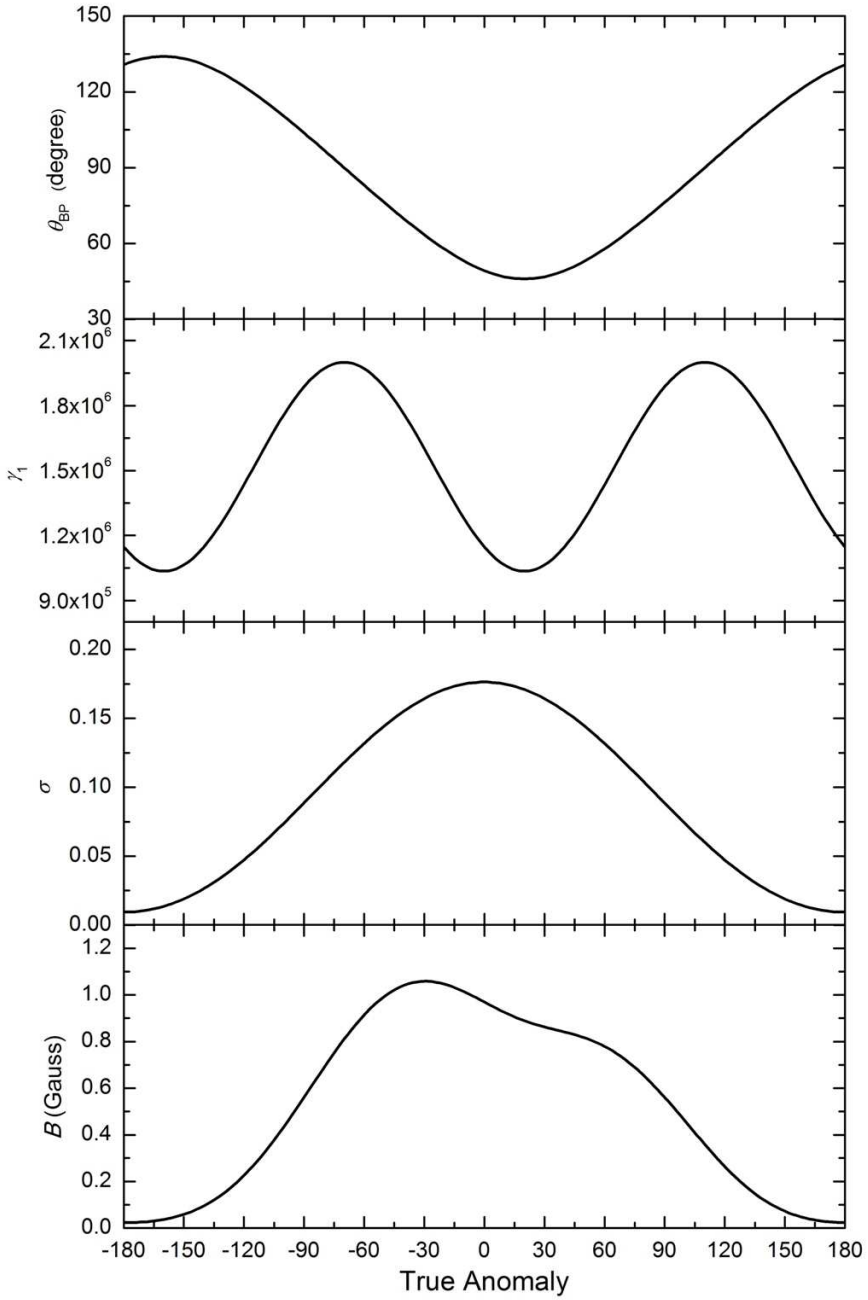

Fig. 2.— From top to bottom: the variations of the angle between the pulsar spin axis and the line joining the two stars $\theta_{\rm BP}$, the bulk Lorentz factor of the unshocked pulsar wind γ_1, the magnetization parameter at the termination shock σ and the magnetic field around the shock apex B with respect to the orbital phase.

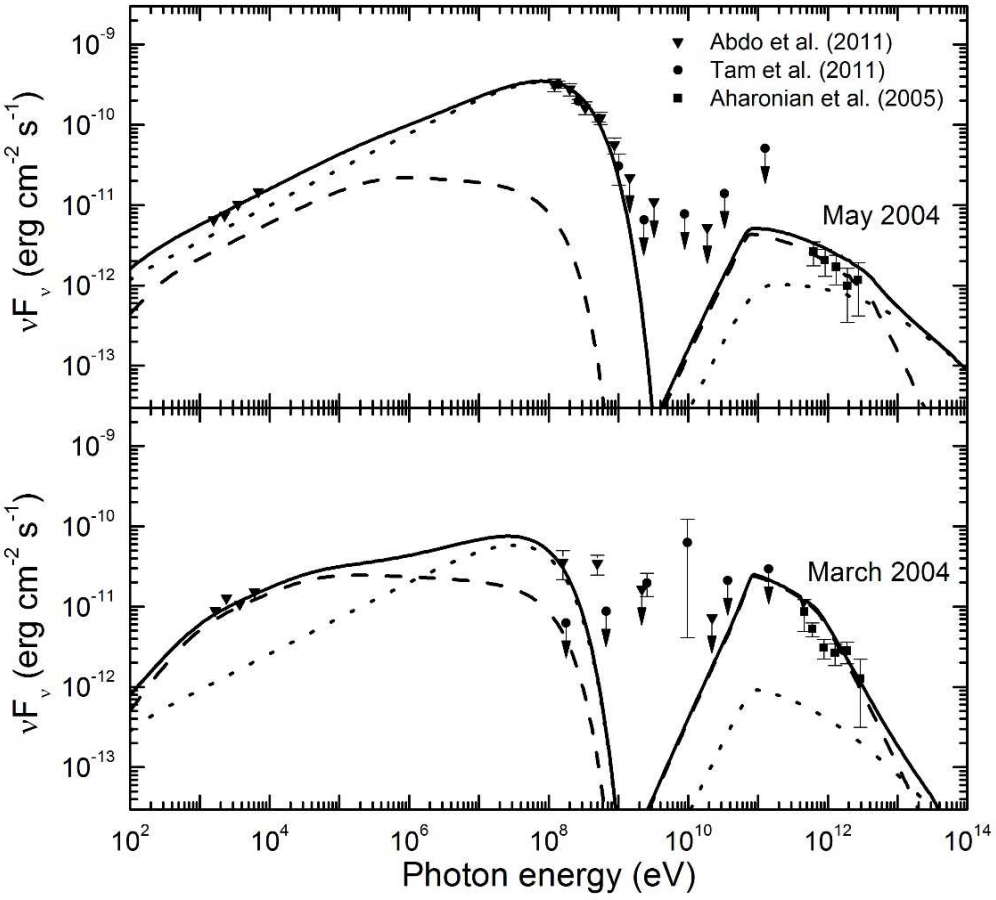

Fig. 3.— The calculated spectra as compared with observations. The spectrum data are taken from Aharonian et al. (2005), Abdo et al. (2011) and Tam et al. (2011). In the upper panel, the spectra are calculated at true anomaly of 120^o and the data are taken in the post-periastron range. In the lower panel, the spectra are calculated at true anomaly of -60^o and the data are taken in the pre-periastron range. The dashed lines and dotted lines correspond to the emission from the shock apex and shock tail respectively, and the solid lines correspond to the total flux.

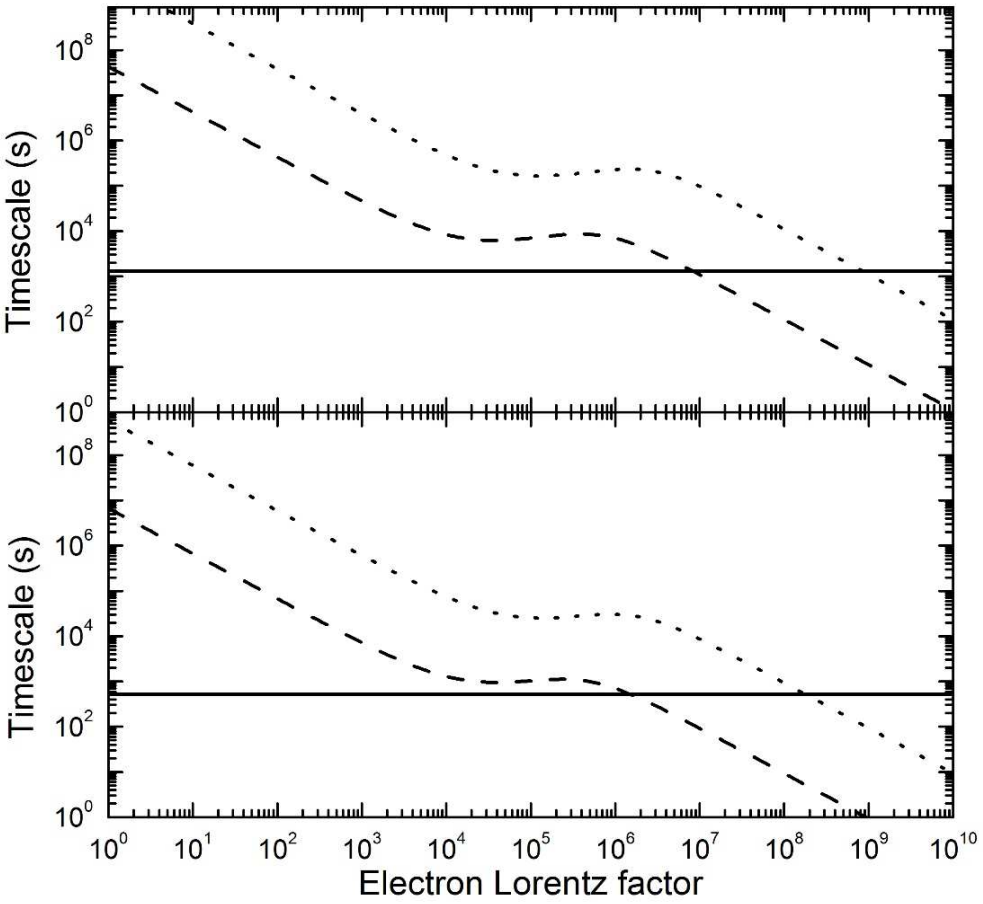

Fig. 4.— The calculated timescales with respect to the electron energies. The solid lines correspond to the dynamical timescale $\tau_{\rm dyn}$, the dashed lines and dotted lines correspond to the cooling timescales $\tau_{\rm c}$ in the shock apex and shock tail respectively. In the upper panel, the timescales are calculated at true anomaly of 120$^{\rm o}$, and in the lower panel, the timescales are calculated at true anomaly of $-60^{\rm o}$.

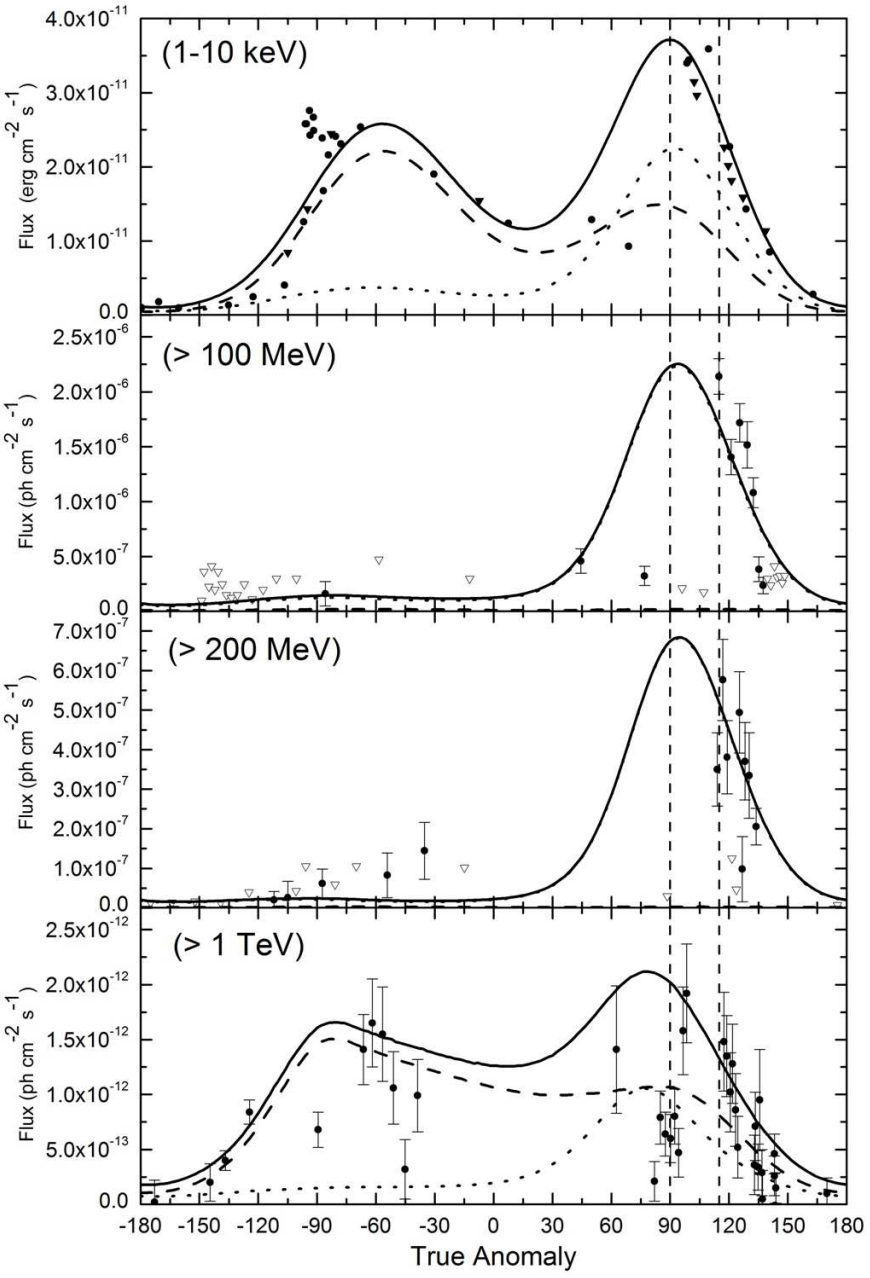

Fig. 5.— The calculated multi-band light curves as compared with observations. The X-ray light curve data are taken from Chernyakova et al. (2006, 2009; circles) and Abdo et al. (2011; triangles), the > 100 MeV light curve data are taken from Abdo et al. (2011), the > 200 MeV light curve data are taken from Tam et al. (2011) and the TeV light curve data are taken from Aharonian et al. (2005, 2009). The dashed lines and dotted lines correspond to the emission from the shock apex and shock tail respectively, and the solid lines correspond to the total flux. The empty triangles are upper limits in observations. The vertical dashed lines correspond to the estimated disk passage.